Millisecond-level transient heating and temperature monitoring technique for ultrasound-induced thermal strain imaging

Mengyue Chen[1, *], Zhiyu Sheng[2, *], Ran Wei[3], Bohua Zhang[1, 5], Howuk Kim[1, 6], Huaiyu Wu[1], Yu Chu[1], Qiyang Chen[3], Andrew Breon[4], Sibo Li[5], Matthew B. Wielgat[7], Dhanansayan Shanmuganayagam[7,8,9], Edith Tzeng[10], Xuecang Geng[4], Kang Kim[2, 3, †], Xiaoning Jiang[1, †]

[*] These authors equally contributed to this work

[†] Corresponding author. Email: kangkim@upmc.edu, xjiang5@ncsu.edu

[1]Department of Mechanical and Aerospace Engineering, North Carolina State University, Raleigh, NC, USA

[2]Department of Medicine, University of Pittsburgh, Pittsburgh, PA, USA

[3]Department of Bioengineering, University of Pittsburgh, Pittsburgh, PA, USA

[4]Blatek Inc., Boalsburg, PA, USA

[5]Shenqi Medical (USA) Sirius Technologies Ltd., Boston, MA, USA

[6]Department of Mechanical Engineering, Inha University, Incheon, South Korea

[7]Department of Animal and Dairy Sciences, University of Wisconsin-Madison, Madison, WI, USA

[8]Department of Surgery, University of Wisconsin School of Medicine and Public Health, Madison, WI, USA

[9]Center for Biomedical Swine Research & Innovation, University of Wisconsin-Madison, Madison, WI, USA

[10]Department of Surgery, University of Pittsburgh, Pittsburgh, PA, USA

Abstract

***Background*:** Ultrasound-induced thermal strain imaging (US-TSI) is a promising ultrasound imaging modality that has been demonstrated in preclinical studies to identify a lipid-rich necrotic core of an atherosclerotic plaque. However, human physiological motion, e.g., cardiac pulsation, poses challenges in implementing US-TSI applications, where achieving a millisecond-level temperature rise by delivering acoustic energy from a compact US-TSI probe is a key requirement. This study aims to develop a transient ultrasound heating and thermocouple monitoring technique at the millisecond level for US-TSI applications.

***Methods*:** We designed, prototyped, and characterized a novel US-TSI probe that includes a high-power, 3.5 MHz heating transducer with symmetrical dual 1D concave array. Additionally, millisecond-level temperature monitoring was demonstrated with fast-response thermocouples in laser- and ultrasound- induced thermal tests. Subsequently, we demonstrated the prototyped US-TSI probe can produce a desired temperature rise in a millisecond-short time window *in vitro* phantom and *in vivo* animal tests.

***Results*:** The prototyped US-TSI probe delivered zero-to-peak acoustic pressure up to 6.2 MPa with a 90 V_{PP} input voltage. Both laser- and ultrasound- induced thermal tests verified that the selected thermocouples can monitor temperature change within 50 ms. The fast-response thermocouple confirmed the transient heating ability of the US-TSI probe, achieving a 3.9 °C temperature rise after a 25 ms heating duration (50% duty cycle) in the gel phantom and a 2.0 °C temperature rise after a 50 ms heating duration (50% duty cycle) in a pig model.

***Conclusions*:** We successfully demonstrated a millisecond-level transient heating and temperature monitoring technique utilizing the novel US-TSI probe and fast-response thermocouples. The reported transient ultrasound heating and thermocouple monitoring technique is promising for future *in vivo*

human subject studies in US-TSI or other ultrasound-related thermal investigations.

Keywords: vulnerable atherosclerotic plaque, theranostic ultrasound, ultrasound-induced thermal strain imaging, transient ultrasound-induced heating, transient temperature monitoring

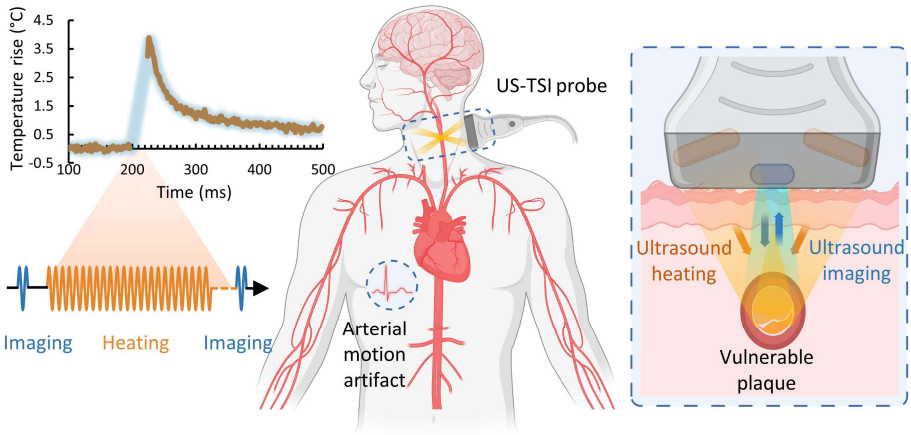

Graphical Abstract

Introduction

Atherosclerosis remains one of the most complex cardiovascular diseases (CVDs) to diagnose, threatening numerous patients' lives [1-5]. The process of atherosclerosis begins with intimal inflammation, necrosis, fibrosis, and calcification at specific artery sites, followed by plaque buildup in the inner lining of arteries, leading to the thickening of artery walls and reduction of blood flow [6-9]. This lessens the oxygen and nutrients reaching the brain (carotid arteries), heart (coronary arteries), and other organs or tissues [10-12]. Atherosclerotic plaques are classified as stable, with a thick fibrous cap and small lipid core, or vulnerable, with a thin fibrous cap and large lipid core. The vulnerable plaque is friable, and the rupture of plaques may diminish blood flow or completely occlude the arteries, leading to sudden cardiac death or acute ischemic stroke. Thus, early detection of subclinical atherosclerosis is crucial for effective prevention of sudden and fatal cardiovascular events [4,13]. To identify vulnerable atherosclerotic plaque, various diagnostic modalities have been proposed, such as invasive and non-invasive approaches [4,14-16]. Typical invasive plaque imaging modalities include intravascular magnetic resonance imaging (IVMRI), intracoronary optical coherence tomography (OCT), intracoronary near-infrared spectroscopy (NIRS), and intravascular ultrasound (IVUS), including the more recent advancement of super-harmonic IVUS [17-23]. Such miniaturized, catheter-based, intravascular imaging modalities provide micrometer-level spatial resolution and offer the capability or potential to visualize plaques prone to rupture. However, these techniques necessitate surgery and have limited accessibility. Of the non-invasive imaging modalities, computed tomography (CT) suffers from limited (millimeter-level) spatial resolution, while magnetic resonance imaging (MRI) is hindered by restricted (centisecond-level) temporal resolution [24-27]. Positron emission tomography (PET) is also effective for early detection of atherosclerosis by assessing molecular-level changes in tissue activity; however, it involves ionizing radiation and costly procedures [28,29].

Ultrasound has demonstrated efficiency and effectiveness in medical imaging, owing to its exceptional spatial and temporal resolution, non-ionizing nature, and affordability. Yet, traditional ultrasound imaging struggles to detect atherosclerotic plaques because the acoustic properties of the plaque closely resemble those of the surrounding tissue. However, the ultrasound-induced temperature rise within the tissue leads to differential changes in sound speed within lipid- and water-bearing tissues, allowing for the distinction of lipid-laden tissue from the surrounding tissue primarily composed of

water. As vulnerable atherosclerotic plaques have higher proportions of lipids within the core, such plaques can be identified by 1) recording the ultrasound radiofrequency data before and after the induced temperature rise, 2) tracking the temperature rise-induced echo shifts change in time of flight, and 3) calculating the apparent strain (i.e., thermal strain or temporal strain) [30,31]. This offers a new capability by utilizing ultrasound for the initial heating and subsequent imaging of vulnerable atherosclerotic plaque. Such innovative theranostic modality, merging therapeutic ultrasound with diagnostic ultrasound, is referred to as ultrasound-induced thermal strain imaging (US-TSI) [32,33].

The development of US-TSI dates back a decade and a half when Huang et al. first demonstrated the feasibility of inducing and imaging thermal strain using a commercial ultrasound scanner in a gelatin phantom with a cylindrical rubber inclusion [30]. Kim et al. further proved the potential of US-TSI for detecting and monitoring atherosclerotic plaque using rabbit kidneys *ex vivo* [34]. The first *in vivo* animal (rabbit) studies by Mahmoud et al. confirmed that US-TSI can monitor lipids in atherosclerotic plaque [31]. Besides these studies, work has been done to enhance the performance of US-TSI devices by developing high-powered US-TSI systems to increase heating speed, employing advanced ultrasound beamforming algorithms to enlarge heating volume, or implementing compensation algorithms to mitigate physiological motion artifacts. For example, Stephens et al. developed a novel US-TSI probe consisting of six 3.5 MHz heating transducers, which can produce a 3 °C temperature in 2 s [35]. Nguyen et al. and Khalid et al. employed a multi-focus beamforming algorithm on a linear array and a curved linear array, respectively, to achieve a relatively large and uniform heating area within a few seconds [36,37]. Yin et al. proposed and refined a compensation method to prevent artifacts caused by respiration within seconds [38,39]. In summary, current US-TSI devices, particularly concerning their heating performance (Table S1), are better suited for mitigating physiological motion artifacts such as those caused by respiration rather than cardiac pulsation. Further improvements are necessary to optimize US-TSI devices for clinical applications where physiological motion (e.g., cardiac pulsation) exists. The displacement of arterial wall motion within a 1/8th cardiac cycle, lasting 75 - 125 ms, is generally less than 1 mm and thus practical for plaque imaging [40]. Additionally, major human arteries, like the carotid, are typically 4 - 7 mm in diameter [41]. This necessitates generating a 10 × 10 mm^2 heating area to cover the artery adequately. Thus, the desired US-TSI device must heat a 2 × 10 × 10 mm^3 volume and produce an approximately 2 °C increase within 50 ms (Figure 1) [42].

After the desired US-TSI prototype is developed, it's essential to monitor transient temperature changes within biological tissue to validate its rapid heating performance. Infrared (IR) thermometry, magnetic resonance (MR) thermometry, and thermocouple thermometry are mainly used for biological temperature monitoring. However, IR thermometry utilizes the emitted infrared radiation from objects to assess temperature variations, limiting its capabilities to measure surface temperatures [43]. MR thermometry exploits the proton resonance frequency shift to evaluate the temperature change deep inside the body; however, it lacks the capability of transient temperature monitoring due to second-level temporal resolution [44,45]. Thermocouple thermometry relies on the Seebeck effect, where a potential is generated when two dissimilar metals in contact are exposed to temperature change [46]. These attributes of simplicity, versatility, and durability have contributed to the widespread adoption of thermocouples in various temperature monitoring applications. Importantly, thermocouples exhibit rapid response times, reaching temporal resolutions on the order of milliseconds [47]. This quality demonstrates their potential for validating the transient heating performance of US-TSI devices.

The principal objective of this study is to develop techniques for millisecond-level transient ultrasound heating and thermocouple monitoring tailored for US-TSI applications. A novel US-TSI probe equipped with a high-power heating transducer was designed, simulated, fabricated, and characterized. The feasibility of transient temperature monitoring approaches was demonstrated using commercial ultra-fast response thermocouples in experiments involving laser- and ultrasound- induced heating. Finally, we conducted *in vitro* phantom and *in vivo* animal tests to showcase the viability of inducing transient heating with the prototyped US-TSI probe.

Materials and Methods

US-TSI Probe System

The US-TSI probe aims to provide satisfactory heating capabilities in speed and volume and image the human carotid artery with sufficient spatial and temporal resolution. As illustrated in Figure 1, the probe is mainly comprised of an imaging transducer (blue part) and a heating transducer (orange part). The imaging transducer is a 1D linear array consisting of 192 elements, whereas the heating transducer is a symmetrical dual 1D concave array consisting of 16 elements for each side. The imaging transducer and heating transducer are linked to a Verasonics ultrasound system (Vantage 256™, Verasonics Inc., WA, USA) with an external power supply for pulse sequence control. The external power supply (QPX600DP, Aim and Thurlby Thandar Instruments, Ltd., UK) supports a maximum input voltage of 190 V_{PP}, an average power of up to 1200 W, and a maximum current of 2.0 A per channel for pulse lengths lasting up to several seconds. To elevate the temperature in the region of interest, the heating transducer delivers a pulse train with a duty cycle of 50 % that overall lasts less than 50 ms, and there are 240 cycles in each pulse. The pulse from the imaging transducer has only 2 cycles for each transmit and it captures the echoes both before and after the heating sequences. The driving voltage is kept constant to avoid repeatedly charging and discharging of the hardware capacitor during short periods. In this way, the imaging and heating transducer have to share the same driving voltage that is much higher than needed for the imaging array. Therefore, a programmable apodization was applied to the imaging array to scale down the transmit power. Based on our previous studies, the center frequency of the heating transducer is set at 3.5 MHz to strike a balance between the required ultrasound penetration depth and the desired acoustic energy absorption [35]. We also applied the dual focal depth method on the heating transducer to enlarge the ultrasound beamwidth. The lateral focal depth was set at 40 mm (YZ-plane) based on phase delay, while the elevational focal depth was set at 60 mm (XZ-plane) based on curvature radius [42]. Other design specifications are summarized in Table I.

Heating Transducer Design and Simulation

The primary innovation of the US-TSI probe lies in the development of a heating transducer exhibiting superior temperature elevation performance. In our previous study, we preliminarily designed the heating transducer by simulating the ultrasound beam pattern and temperature response [42]. The simulated results demonstrated that the designed heating transducer generally meets the heating volume and speed requirements. We further developed the heating transducer in the present study by determining the acoustic lens and phase delay.

Figure 1B depicts the design layout of the US-TSI probe, where the symmetrical dual heating arrays are situated 30 mm apart on both sides of the imaging array. Each heating array rotates 25° to target the location 25 mm below the imaging array. Furthermore, compared to the previous design, we chose PZT-5A instead of PZT-4 as active materials and selected dual 1D arrays instead of dual 1.5D arrays as the transducer configuration [42]. This new design enlarged the size of each heating array element and electrically connected the five sections in one channel to achieve a reduced electrical impedance approaching 50 Ω. The soft piezoelectric material, PZT-5A, was selected as the active material for heating array elements owing to its high piezoelectric constants and mechanical strength, with Al_2O_3/epoxy and air as the materials for the matching and backing layers, respectively. A concave acoustic lens, constructed from graphite and having a radius of 41 mm, was also attached to the surface of the heating transducer to avoid side lobes. To obtain a larger volume for the heating zone, the multi-focus beamforming technique was implemented on the heating transducer by programming phase delays on each heating element [36].

The ultrasound beam pattern of the designed heating transducer, especially with an acoustic lens and phase-delay algorithm, was optimized and confirmed using finite element simulation to make sure the focal area can cover human carotids with a diameter of 4 - 7 m. Due to the massive computational cost, we only simulated acoustic pressure distribution using COMSOL Multiphysics (6.1, COMSOL Inc., Stockholm, Sweden) in a 2D plane. The acoustic-piezoelectric model is illustrated in Figure S1,

and the corresponding simulation parameters are summarized in Table S2 [48-50]. To determine the phase delay on each element, we followed our previous study, which showed that the delay profile for a linear array transducer generally exhibits a parabolic shape with two distinct notches or dips near the peak [36]. To apply phase delay in the finite element simulation, we first calculated the time delay between each element, then converted the time delay to phase delay, and finally applied the input voltage of each element using a complex-valued number (Figure S1). By checking the simulated ultrasound beam pattern, we selected the appropriate phase delays of each element, illustrated in Figure S1.

Heating Transducer Fabrication and Characterization

We first prototyped three single heating transducer elements with three materials: PZT-5A, PZT-5H, and PMN-PT. After conducting characterization consisting of electrical impedance, pulse-echo, and hydrophone tests, we adopted PZT 5A as the active layer due to its superior loop and transmitting sensitivities. Detailed comparisons are summarized in Table S3. The matching layer was fabricated by mixing Al_2O_3 powder (ALR-1005-01, Pace Technologies Inc., AZ, USA) and epoxy resin (EPO-TEK 301, Epoxy Technology, Inc., MA, USA), while the backing layer was prepared using the mixture of air-bubble powder (Blatek Industries, Inc., PA, USA) and epoxy resin (EPO-TEK 301, Epoxy Technology, Inc., MA, USA). Then, a 10-μm thick Parylene-C layer was coated to encapsulate the heating transducer for waterproofing. Finally, we integrated the heating and imaging transducer into a 3D printing housing according to the design layout to prototype the US-TSI probe.

After the fabrication of the US-TSI probe, we measured the electrical characteristics of each heating transducer element, including the impedance and phase spectrum, by a precision impedance analyzer (4294A, Agilent Technologies Inc., CA, USA). The output and distribution of its acoustic pressure were measured using a hydrophone to assess the acoustic characteristics of the prototyped US-TSI probe. As illustrated in Figure 2A, a water tank filled with degassed water was utilized to accommodate both the US-TSI probe and the hydrophone. Verasonics ultrasound system was used to control the US-TSI probe. Specifically, a sinusoidal pulse of 10 cycles per 1 ms was transmitted to drive the heating transducer. A calibrated bullet hydrophone (HGL-0085, ONDA Corporation, CA, USA) connected with a 20 dB preamplifier (AH-2020, ONDA Corporation, CA, US) was placed in the region of interest behind the heating transducer. Given that the bullet hydrophone could not measure high-pressure/intensity ultrasound, we operated the heating transducer with input voltages ranging from 0 to 20 V_{PP}. The measurement was repeated three times for each input voltage to obtain averaged acoustic outputs. The acoustic pressure field was acquired and recorded using a digital oscilloscope (DSO7104B, Agilent Technologies, Inc., CA, USA) with the assistance of the 3-axis positioning system. Specifically, we conducted scans of the acoustic pressure distribution in the XZ and YZ planes, employing a step size of 0.5 mm in the X and Y directions and 1.0 mm in the Z direction. In addition, we measured zoom-in acoustic pressure fields along the X and Y directions with a step size of 0.1 mm.

Thermocouple Preparation and Verification

We opted for commercially available thermocouples with milliseconds response time to capture the transient temperature change. In selecting thermocouple types, we chose Type T (copper-constantan) due to its exceptional accuracies (approximately 1.0 °C) and ample temperature ranges (-250 to 350 °C) compared to Type J, K, and E. To record the signal from the thermocouple, we connected a data acquisition (DAQ) module (OM-DAQ-USB-2401, Omega Engineering, Inc., CT, USA) to the thermocouple, operating at a sampling rate of 500 Hz. Other details of two selected thermocouples utilized in this study are summarized in Table S4.

To verify the capability of selected thermocouples, we need robust and stable heating sources known to deliver a comparable amount of energy and produce a similar temperature to the new US-TSI probe. In this paper, we used a laser line generator to perform the heating tests in the air and a single-element ultrasound transducer to perform the heating tests in an excised porcine tissue. As depicted in Figure 2B, a laser line generator driven by a function generator (33250A, Agilent Technologies, Inc., CA,

USA) produced a laser line lasting 50 ms per 2 s. The laser line generator was mounted on a 3-axis motion stage to ensure effective capture of the laser beam by the tip of the thermocouple. The resultant electrical voltage change was recorded by the DAQ system and then translated into a temperature change by the computer.

Regarding the ultrasound-induced thermal tests (see Figure 2B), a single-element ultrasound transducer (Blatek Industries, Inc., PA, USA) was driven by a function generator and an RF power amplifier (75A250A, Amplifier Research Corporation, PA, USA), and generated focused ultrasound waves lasting 50 ms per 2 s. The frequency, acoustic pressure, and focal depth of generated ultrasound waves are 950 kHz, 2.4 MPa, and 20 mm, respectively. A water tank filled with degassed water at 35 °C was employed to house the ultrasound transducer, the thermocouple, and the layers of the porcine tissue. We positioned the thermocouple between two 20 mm-thick porcine tissue layers and mounted the ultrasound transducer on a 3-axis motion stage to ensure effective capture of the ultrasound beam by the tip of the thermocouple.

In Vitro Phantom Tests

Gel phantoms with a gelatin concentration of 5% (w/v gelatin powder/saline) were prepared to mimic biological tissue. 25 g gelatin powder (G2500, MilliporeSigma Corporation, MA, USA) was first added to 500 mL phosphate-buffered saline (PBS) solution (Gibco, Thermo Fisher Scientific Inc., MA, USA) at 49 °C using a stirring hot plate (PC420D, Corning Inc., NY, USA). Afterward, we carefully removed any trapped air bubbles within the solution and stirred it thoroughly with a magnetic stirrer until the gelatin was dissolved completely. The solution was then cooled to 38 °C and mixed with 5 g of cellulose powder (S3504, MilliporeSigma Corporation, MA, USA). We subsequently stirred the mixture until fully dissolved and cooled it to 18-21 °C. Finally, the solution was poured into a container and placed in a refrigerator for solidification.

Following the preparation of the gel phantom, we proceeded to perform ultrasound-induced thermal tests using the prototyped US-TSI probe, aided by a fast-response thermocouple for monitoring transient temperature changes. As illustrated in Figure 2C, the US-TSI probe was submerged in a plastic container filled with degassed water and subsequently positioned on the top surface of the gel phantom. This was done to easily eliminate any air bubbles trapped or generated between the US-TSI probe and the gel phantom, as opposed to using ultrasonic couplant gel. In addition, a thin layer of plastic wrap was used to replace the bottom of the plastic container, ensuring adequate transmission of acoustic energy. We inserted the fast-response thermocouple into the region of interest of the gel phantom, which is about 35 mm below the heating transducer and 25 mm below the imaging transducer. Furthermore, a controller linked to a computer was employed to synchronize the Verasonics system and the DAQ system. The Verasonics ultrasound system operated the heating transducer with different input voltages, ranging from 40 V_{PP} to 90 V_{PP}, for a duration of 25 ms. The DAQ system recorded the electrical voltage change of the fast-response thermocouple at a sampling rate of 500 Hz. It should be noted that each condition was repeated three times, and the results were averaged to ensure reliable temperature monitoring.

In Vivo Animal Tests

The animal test was performed on a Wisconsin Miniature Swine™ (WMS™) to validate the effectiveness of the US-TSI probe-induced temperature increase *in vivo*. Under a protocol approved by the Institutional Animal Care and Use Committee (IACUC) at the University of Pittsburgh, the pig was anesthetized and underwent ultrasound imaging and local heating using the prototyped US-TSI probe. As illustrated in Figure 2D, we inserted the fast-response thermocouple under the guidance of ultrasound imaging. Considering the future US-TSI applications on the human carotid artery at a similar depth to a pig femoral artery under the skin, we targeted a homogenous muscular area near the femoral artery of the left leg. The US-TSI probe, filled with ultrasonic couplant gel and covered using a very thin plastic wrap (Figure S2), rested on the pig leg using a probe holder. We adjusted the position of the US-TSI probe and used visual feedback from ultrasound imaging to ensure the precise positioning of the thermocouple. To demonstrate and compare the effectiveness of the acoustic

heating, we executed the acoustical heating sequence using the Verasonics ultrasound system with an external power supply as used in the previously mentioned phantom tests and recorded temperature curves when the tip of the thermocouple was identified at three different locations (0, 2, 5 mm off focus). The temperature data was stored using the DAQ system. The Verasonics ultrasound system operated the heating transducer with an input voltage of 90 V_{PP}, a pulse cycle of 240, a duty cycle of 50%, and a heating duration of 50 ms. The DAQ system recorded the electrical voltage change of the fast-response thermocouple at a sampling rate of 500 Hz.

Results

Heating Transducer Development

Figure S3 illustrates the simulated acoustic pressure fields of the heating transducer in the YZ plane, which consisted of various conditions, including the presence and absence of acoustic phase delay and acoustic lens. All the simulated acoustic pressure fields were normalized to the peak pressure of each ultrasound beam. It was observed that using both the acoustic lens and phase delay is essential to prevent wide, unfocused beam patterns (Figure S3A), low acoustic pressure (< -20 dB) between focal points (Figure S3B), and a focal area shift above the region of interest (Figure S3C). Additionally, we selected the phase delay illustrated in Figure S1 to get an approximately 8 x 16 mm^2 focal area (-12 dB) illustrated in Figure S3D and Figure S4, which fully cover human carotids with a diameter of 4 - 7 mm. It was also noted that when the axial distance is less than 13 mm, the sound pressure level (SPL) drops below -30 dB (Figure S3D). Therefore, we opted to position the imaging array at an axial distance of 10 mm. Using the optimized design verified by simulated results, the US-TSI probe was prototyped accordingly (refer to Figure 1).

Heating Transducer Characterization

Figure 3 illustrates the electrical and acoustic characteristics of the prototyped heating transducer. The capacitance and dielectric loss at 1 kHz for the 32 heating transducer elements were 1.04 ± 0.04 nF and 11.71 ± 0.61 mU, respectively. Meanwhile, the electrical impedance at operating frequency (i.e., 3.5 MHz) and minimum impedance frequency for the 32 heating transducer elements were 36.65 ± 6.14 Ω and 3.55 ± 0.17 MHz. The detailed electrical characteristics of each heating transducer element are displayed in Figure 3A&B and Table S5. In Figure 3C, the zero-to-peak acoustic pressure and spatial-peak pulse-average acoustic intensity (I_{SPPA}) were depicted in blue and orange colors, respectively. We extrapolated acoustic pressure and intensity by applying linear and 2^{nd}-order polynomial trendlines, respectively. The result indicated that an input voltage of 90 V_{PP} applied to the heating transducer could generate approximately a peak pressure of 6.2 MPa and an I_{SPPA} of 1300 W/cm^2. Figures 4D and 4E display the measured acoustic pressure fields of the heating transducer in the XZ and YZ planes. It should be noted that the axial distance in Figures 4D and 4E refers to the distance between the hydrophone and the imaging transducer. Spline interpolation was employed to enhance the smoothness of the map depicting the normalized acoustic pressure field. The measured results in Figures 4D and 4E show that the focal depth of the heating transducer was at the axial distance of 25 mm, aligning with the design objectives. The -12 dB beamwidth was measured to be about 2 mm in the X-direction and 10 mm in the Y-direction. It is clear that an ultrasound beam pattern resembling an “X” shape, as shown in Figure 4E, was formed due to the configuration of symmetrical dual heating arrays. Figures 4F and 4G present the zoomed-in acoustic pressure distribution, expressed as SPL, in the X- and Y-directions at a focal depth of 25 mm. It is interesting to observe multiple crests and troughs occurring in the Y-direction. In addition, as illustrated in Figures 4H and 4I, we plotted the spatial acoustic pressure distribution (at a focal depth of 25 mm) along the X-axis and the temporal acoustic pressure distribution (including a time window of 10-cycle tone burst) along the Y-axis. These temporal-spatial acoustic pressure distributions for both the lateral and elevational directions displayed the acoustic wave propagation and interference from the dual ultrasound heating transducer array.

Thermocouple Verification

Figure S5 illustrates the representative temperature curves in both laser-induced and ultrasound-induced thermal tests. It can be observed, from the raw data dots, that the variation in temperature changes is approximately 0.7 °C in the air and 0.9 °C in the tissue. Thus, a moving average (over 10 periods) was applied during the signal processing to mitigate noise effects and measurement variations. From the moving average line, it is noticeable that a temperature peak occurs every 2 s, with each temperature rise lasting about 50 ms for each peak. This is in accordance with the set period of laser/ultrasound pulse width and pulse repetition period. This result indicated that the selected thermocouples can be used to monitor millisecond-level trainset temperature.

In Vitro Phantom Tests

We performed in vitro phantom tests using the prototyped US-TSI probe after heating transducer characterization and thermocouple verification. The B-mode image captured by the imaging transducer is presented in Figure 4A, wherein the thermocouple is marked by a circle. Notably, the bright line at the top (indicated by an arrow) represents the boundary between the gel phantom with scatterers and the water contained by a layer of plastic wrap. Figure 4B illustrates the transient temperature changes during a 500 ms period in a plot of normalized temperature over time. It is important to note that due to the strong electromagnetic interference from the prototyped US-TSI probe, we removed the corresponding error data and marked the affected period using a diagonal stripe pattern. It can be observed that applying an input voltage of 90 V_{PP} on the heating transducer can cause a temperature rise of 3.9 °C after a 25 ms heating duration. The corresponding acoustic pressure and intensity at the heating focal zone were approximately estimated as 6.2 MPa and 1300 W/cm^2, respectively, based on the heating transducer sensitivities depicted in Figure 3C. While the detailed temperature curve within the 25 ms heating duration cannot be observed due to intense electromagnetic interference, it is evident that higher input voltage contributed to higher transient temperature rise. We then plotted the relationship between normalized temperature, acoustic pressure, and intensity, as shown in Figure 4C and Figure 4D. The error bars for the temperature rise correspond to the standard deviations across three repeated thermocouple measurements. There appears to be a linear dependence between the temperature rise and the acoustic intensity. The deviation between the measured data dots and estimated trend line might be attributed to (i) estimation error in predicting acoustic intensity in gel phantom rather than water and (ii) measurement error in placing the thermocouple in the focal zone of the ultrasound heating beam.

In Vivo Animal Tests

The animal test results are presented in Figure 4. Figure 4E illustrates the B-mode images captured by the imaging transducer for three different thermocouple locations, wherein the thermocouple is marked by a red circle. The three thermocouple locations included one "at focus" case, positioned at the focal spot of the heating beam, and two "off focus" cases, positioned at 2 mm and 5 mm laterally off the focus. Figure 4F illustrates the corresponding transient temperature changes for the three thermocouple locations before and after the ultrasound heating. Like the previous phantom test results, the real temperature curve within the 50 ms heating duration cannot be monitored due to intense electromagnetic interference from the US-TSI probe. However, it is noteworthy that the temperature can rise roughly 2 °C after a 50 ms heating duration for both “0 mm off” (i.e., at focus) and “2 mm off”, indicating that the effective heating zone is larger than 4 mm in the lateral direction of the imaging transducer. For the thermocouple location of “5 mm off”, it is hard to observe any obvious temperature changes, indicating that the heating beam does not heat surrounding tissue outside the heating region of interest. Considering that the design requirement for the heating area size in the lateral direction of the imaging transducer is within 2 mm, these results demonstrate that the prototyped US-TSI probe delivers sufficiently high power for transient heating uniformly only within the target area, reflecting the effectiveness and safety for *in vivo* applications.

Discussions

This study sought to develop a millisecond-level transient ultrasound heating and thermocouple monitoring technique for US-TSI applications. We first designed, prototyped, and characterized a novel US-TSI probe that included a heating transducer with exceptional heating capabilities. The simulation results, in terms of the acoustic pressure field in the YZ plane (Figure S3), emphasize the importance of applying an acoustic lens and a multi-focus beamforming algorithm. These measures can enlarge and homogenize the focal zone of the ultrasound heating beam. However, it should be acknowledged that the absence of 3D finite element simulation, attributable to substantial computational costs, posed challenges in the design of the heating transducer. Consequently, we opted for a compromise by (i) initially conducting a 3D acoustic simulation using Field II to validate the design specifications of the heating transducer in the previous study [42] and (ii) subsequently performing a 2D acoustic simulation using COMSOL to confirm the layout and phase delay of the heating transducer in the current study.

Regarding the acoustic characterization of the heating transducer, the measured transducer sensitivity aided us in estimating that the acoustic pressure of the prototyped US-TSI probe could reach 6.2 MPa (Figure 3C) when applying a 90 V_{PP} input voltage to the heating transducer. The measured pressure indicated the capability of delivering sufficient energy quickly. Ultimately when applying US-TSI in the clinical setting, this driving voltage needs to be scaled down to satisfy Food and Drug Administration (FDA) safety limits [51]. For the acoustic pressure field shown in Figure 3E, the multi-focus beamforming and acoustic lens contributed to a wider beamwidth in the Y-direction compared to the X-direction. It is promising to see that the -12 dB beamwidth is roughly 10 mm, which is capable of heating major human arteries. Also, the multiple crests and troughs in both the X- and Y-directions are believed to be induced by ultrasound wave interference from the dual heating arrays (Figures 3D&E and Figure S4). The measured distance between the two neighboring crests/troughs is about 0.6 mm, which is closely aligned with the calculated value according to the fringe spacing equation for two-plane wave interference: $d_f = \frac{\lambda}{sin\,\theta} = \frac{0.42\,mm}{sin\,50°} \approx 0.55\,mm$, where d_f is known as the fringe spacing, λ is the wavelength, and θ is the wave interference angle. In addition, considering that the conventional evaluation method for acoustic pressure field only accounts for the maximum ultrasound pressure in the spatial domain, we also involve the temporal acoustic pressure information to better observe the ultrasound wave propagation from the heating transducer. The normalized acoustic pressure field illustrated in Figures 3H and 3I reveal the interference patterns of ultrasound waveforms from the dual heating arrays, highlighting how the acoustic pressure varies with time and space. This new spatial-temporal evaluation metric might be promising for the acoustic characteristics of therapeutic ultrasound transducers in the future.

Apart from prototyping and characterizing the heating transducer, the approach for milliseconds-level temperature monitoring was also successfully demonstrated (Figure S5). This approach holds promise for future biological-related thermal studies such as TSI-based tissue characterization, TSI-based temperature monitoring, and ultrasound-induced thermal ablation [32,33,52]. Nevertheless, it should be acknowledged that thermocouple thermometry has its drawbacks for ultrasound-induced thermal studies. The power cable of the ultrasound transducer needs to be carefully shielded and grounded to prevent the potential capacitive coupling effects. If not, the induced electromagnetic interference might disturb the thermocouple and induce “pick-up” errors [53]. Moreover, evaluation of the impact of viscous heating artifacts on thermocouples is challenging, particularly for millisecond-level temperature monitoring [54]. Addressing this issue will require further research and effort in the future.

Finally, utilizing the fast-response thermocouple, we successfully demonstrated the ability of the prototyped US-TSI probe to induce millisecond-level temperature changes in both a tissue-mimicking gel phantom and a muscular region near the femoral artery of a pig. In the *in vitro* tests, the heating transducer increased the temperature by 3.9 °C after a 25 ms sonication duration, suggesting a satisfactory heating capability and the margin for tuning *in vivo* to meet both heating and safety requirements. The *in vivo* tests later showed that the heating transducer enabled a 2.0 °C increase

after a 50 ms sonication duration. The lower temperature rise with a longer heating duration might be due to an energy loss caused by blood perfusion under *in vivo* conditions [55]. We further compared the heating capability of our prototyped US-TSI probe with that of current US-TSI devices, as summarized in Table S1. It can be observed that, with successful *in vitro* and *in vivo* demonstrations, our device advances the transient ultrasound heating capability from second-level to millisecond-level durations, which is promising for mitigating physiological motion artifacts like cardiac pulsation. In addition to heating durations, the performance of our US-TSI probe is also promising in terms of heating volume. A 4 mm effective heating width was observed in the lateral direction of the US-TSI probe (see Figures 4E&F), which is larger than the 2 mm -12 dB beamwidth of the ultrasound (see Figures 3D&F). This raises an interesting question: how can we determine the effective heating width based on the ultrasound beamwidth for millisecond-level duration? Meanwhile, since we could not precisely determine the thermocouple location in the evaluation direction of the US-TSI probe using ultrasound imaging *in vivo*, the effective heating area *in vivo* in that direction remains unknown. However, we expect it to be larger than 10 mm according to the -12 dB ultrasound beamwidth from both numerical simulation and hydrophone measurements. Overall, we remain optimistic about the potential of this novel US-TSI probe for future studies and applications in the field of US-TSI.

The next phases of the project will involve (i) conducting a benchtop investigation using gel phantoms to assess three crucial variables for TSI, namely thermal strain, temperature increase, and lipid concentration; (ii) undertaking an *in-vivo* study involving clinically relevant hyperlipidemic pigs to evaluate the performance and safety of the US-TSI probe and optimize the US-TSI protocol for clinical translation; (iii) initiating a pilot human study involving patients with atherosclerosis to demonstrate the capability of US-TSI in detecting plaque in the human carotid artery.

Conclusions

To the best of our knowledge, this study marks the first successful demonstration of a millisecond-level transient heating and temperature monitoring technique in US-TSI. In this study, a novel US-TSI probe was developed, showcasing remarkable heating capabilities. The performance of the heating transducer was assessed by examining its acoustic pressure output and distribution. Additionally, an approach for transient temperature monitoring using fast-response thermocouples was established. Following that, we demonstrated that the prototyped US-TSI probe can induce millisecond-level transient heating. It is believed that the developed millisecond-level transient ultrasound heating and thermocouple monitoring technique is promising for future studies in the US-TSI field or other ultrasound-related thermal effects investigations.

Acknowledgments

The work was supported by the National Institutes of Health (NIH) under award number R01HL152023.

Tables and Figures

TABLE I DESIGN SPECIFICATIONS FOR THE US-TSI PROBE

Imaging Transducer		Heating Transducer	
Configuration	1D Linear Array	Configuration	Dual 1D Concave Arrays
Elements number	192	Elements number	2 x 16
Element pitch (X-direction*)	0.2 mm	Element pitch (Y-direction*)	1.03 mm
Element kerf (X-direction*)	0.05 mm	Element kerf (Y-direction*)	0.25 mm
Element height (Y-direction*)	4 mm	Element height (X-direction*)	39.75 mm
Center frequency	10 MHz	Center frequency	3.5 MHz
Focal depth	25 mm	Focal depth	60 mm (XZ plane) & 40 mm (YZ plane)
Material	PZT-5H	Material	PZT-5A

*: The lateral and elevation directions of the imaging array correspond to the X- and Y-directions, while for the heating array, the lateral and elevation directions are reversed, corresponding to the Y- and X-directions (Figure 1B).

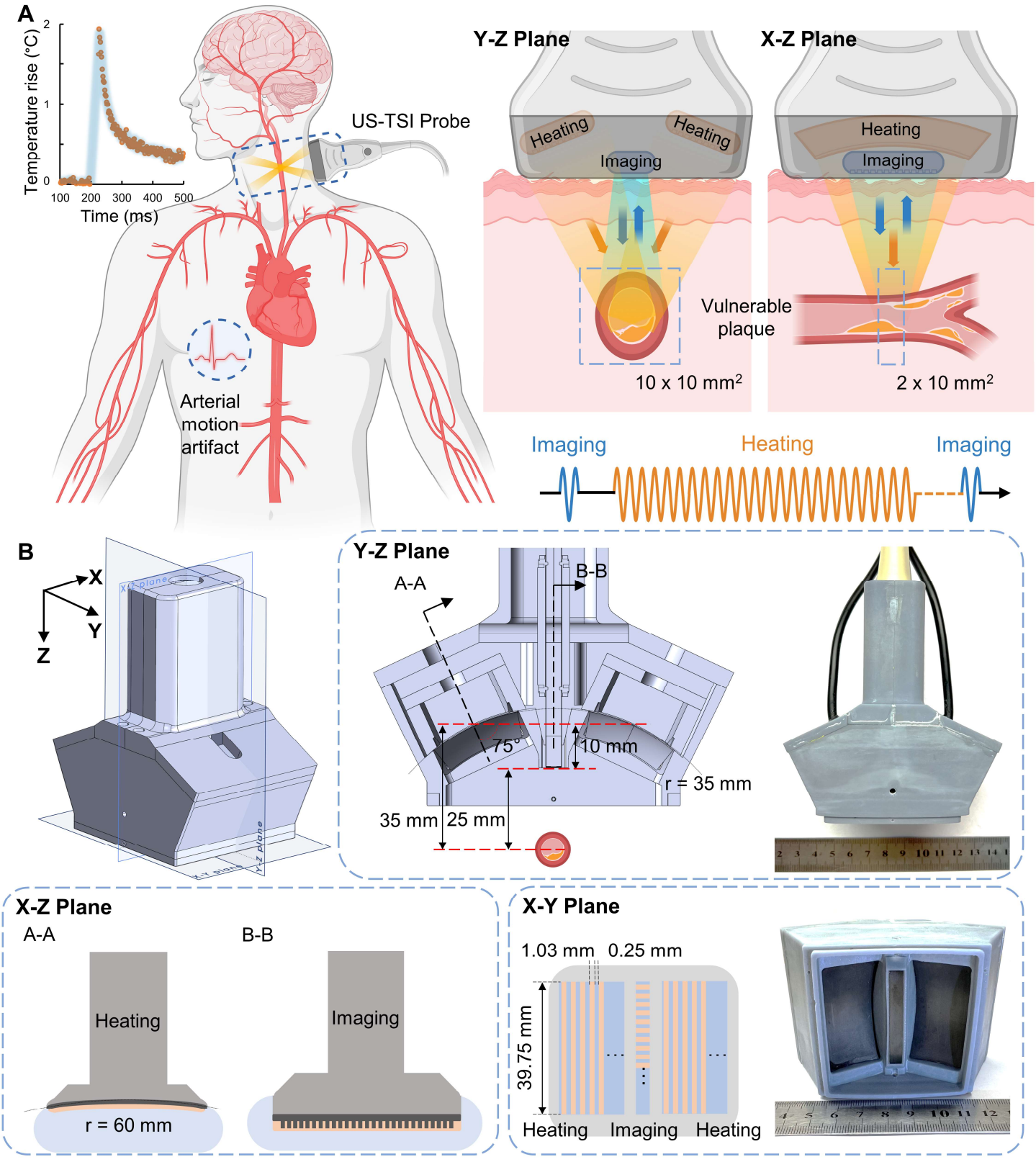

Figure 1. Overview of US-TSI probe for vulnerable plaque detection. (A) Sketch in the short- and long-axis direction for plaque detection using a US-TSI probe in the human artery, with blue arrows/cycles depicting the imaging process and orange arrows/cycles depicting the heating process. **(B)** Schematic and photo of prototyped US-TSI probe, including 3D model and 2D model in XZ, XY, and YZ planes. The figure was partially created by Biorender.com.

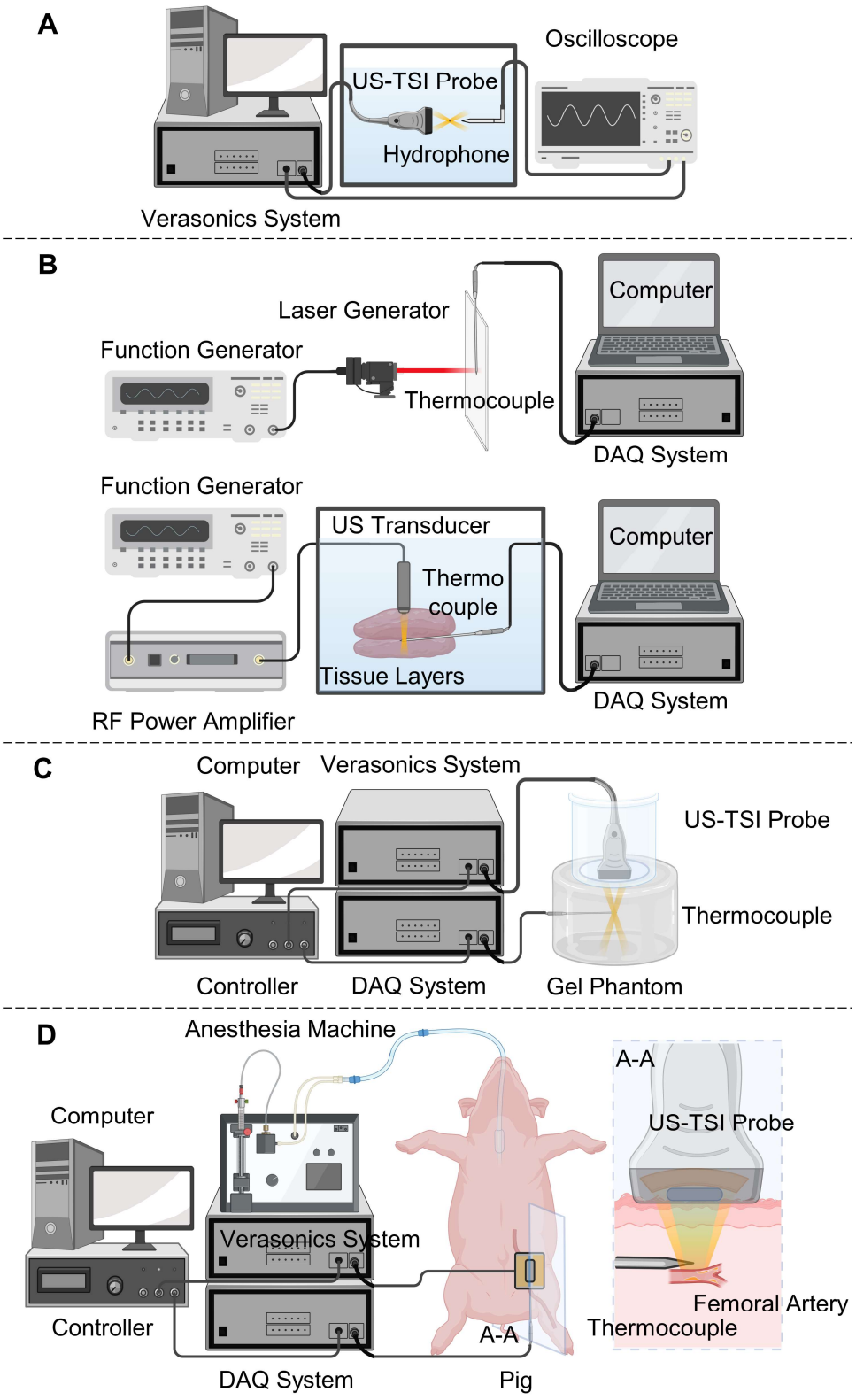

Figure 2. Sketches of experiment setup for **(A)** hydrophone tests to characterize the US-TSI probe; **(B)** laser-induced and ultrasound-induced thermal tests to check the performance of the fast response thermocouples for transient temperature monitoring, **(C)** *in vitro* phantom tests, and **(D)** *in vivo* animal tests to check the transient heating capability of the prototyped US-TSI probe. The figure was created with Biorender.com.

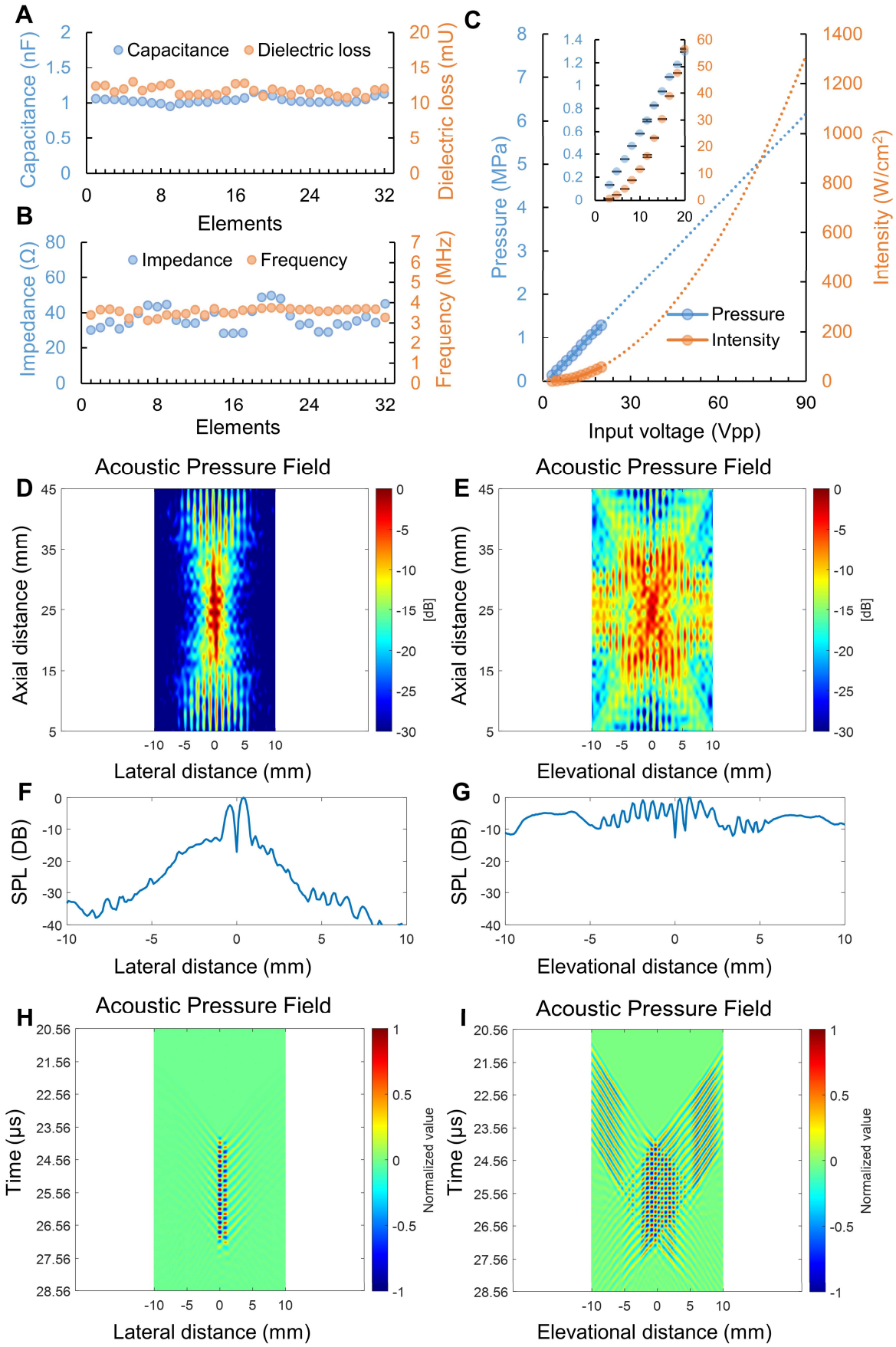

Figure 3. Measured heating transducer characterization results. (A) capacitance and dielectric loss of each heating transducer element at 1 kHz; **(B)** electrical impedance at 3.5 MHz and minimum impedance frequency of each heating transducer element; **(C)** acoustic pressure and intensity output of the heating transducer (n = 3); acoustic pressure filed of the heating transducer in the **(D)** XZ plane and **(E)** YZ plane; zoom-in acoustic pressure distribution

along the **(F)** X- and **(G)** Y-directions; temporal acoustic pressure filed of the heating transducer at focal depth along the **(H)** X- and **(I)** Y-directions.

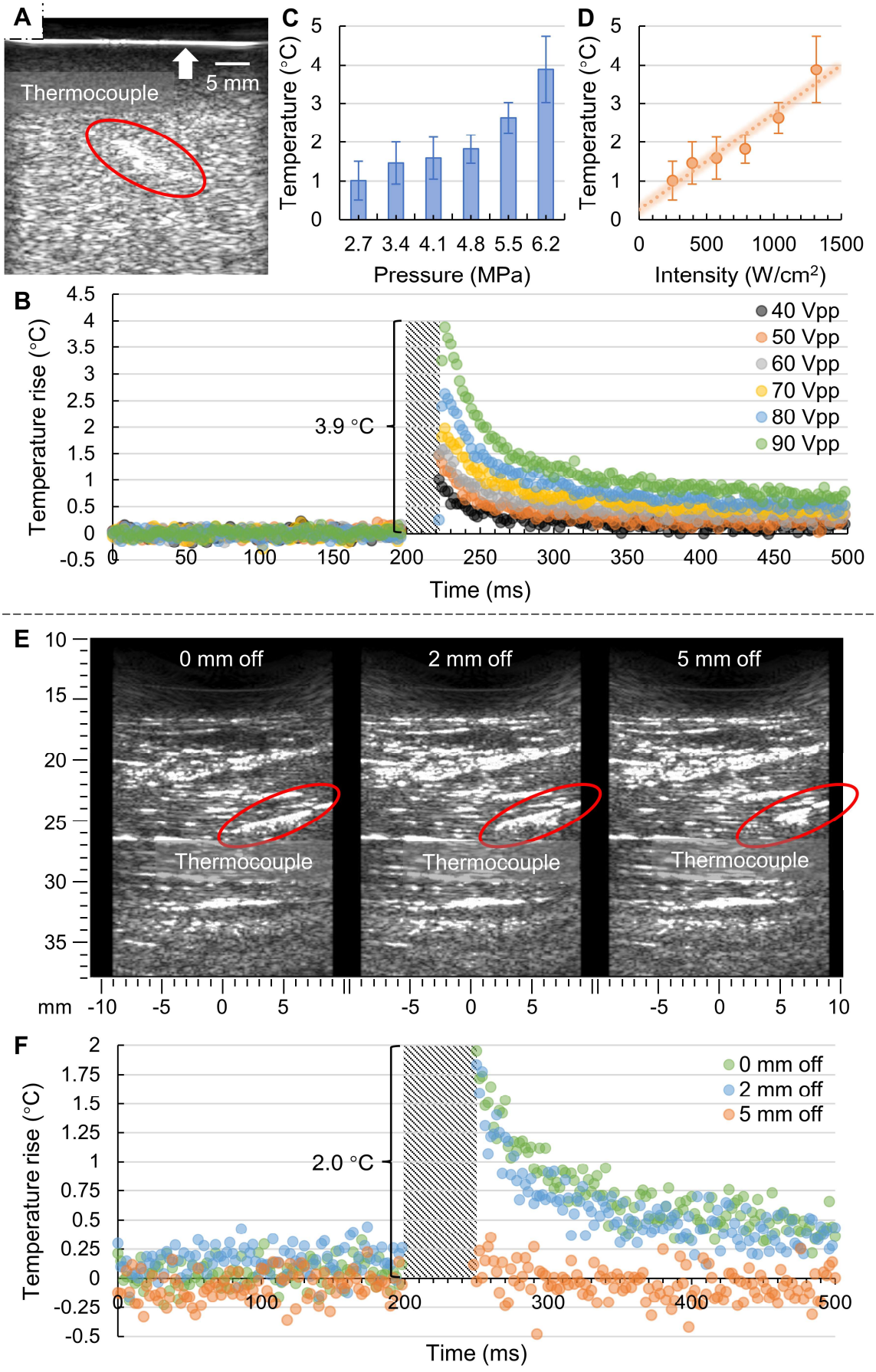

Figure 4. Results of *in vitro* phantom tests and *in vivo* animal tests. (A) B-mode imaging in phantom from the imaging transducer; **(B)** measured transient temperature curve in phantom for various input voltages (n = 3); **(C)** the relationship between temperature rise and acoustic pressure; **(D)** the relationship between temperature rise and acoustic intensity, where the error bar represents the standard deviation from three repeated measurements (n = 3); **(E)** B-mode imaging in pig leg shows thermocouple locations; and **(F)** measured transient temperature curve in pig leg for three different thermocouple locations (n = 1).

References

1. Kingsbury KJ. Concept of Human Atherosclerosis. Nature. 1969; 224: 146–9.
2. Lusis AJ. Atherosclerosis. Nature. 2000; 407: 233–41.
3. Tsao CW, Aday AW, Almarzooq ZI, et al. Heart Disease and Stroke Statistics—2023 Update: A Report From the American Heart Association. Circulation. 2023; 147: E93–621.
4. Fayad ZA, Fuster V. Clinical Imaging of the High-Risk or Vulnerable Atherosclerotic Plaque. Circ Res. 2001; 89: 305–16.
5. Naghavi M, Libby P, Falk E, et al. From Vulnerable Plaque to Vulnerable Patient. Circulation. 2003; 108: 1772–8.
6. Libby P. Inflammation in Atherosclerosis. Arterioscler Thromb Vasc Biol. 2012; 32: 2045–51.
7. Finn A V., Nakano M, Narula J, Kolodgie FD, Virmani R. Concept of Vulnerable/Unstable Plaque. Arterioscler Thromb Vasc Biol. 2010; 30: 1282–92.
8. Bentzon JF, Otsuka F, Virmani R, Falk E. Mechanisms of Plaque Formation and Rupture. Circ Res. 2014; 114: 1852–66.
9. Virmani R, Burke AP, Farb A, Kolodgie FD. Pathology of the Vulnerable Plaque. J Am Coll Cardiol. 2006; 47: C13–8.
10. Kolodgie FD, Burke AP, Farb A, et al. The thin-cap fibroatheroma: a type of vulnerable plaque: The major precursor lesion to acute coronary syndromes. Curr Opin Cardiol. 2001; 16: 285–92.
11. Qureshi AI, Caplan LR. Intracranial atherosclerosis. The Lancet. 2014; 383: 984–98.
12. Banerjee C, Chimowitz MI. Stroke Caused by Atherosclerosis of the Major Intracranial Arteries. Circ Res. 2017; 120: 502–13.
13. Kim H-L, Kim S-H. Pulse Wave Velocity in Atherosclerosis. Front Cardiovasc Med. 2019; 6.
14. Sanz J, Fayad ZA. Imaging of atherosclerotic cardiovascular disease. Nature. 2018; 451: 953-957.
15. Celeng C, Takx RAP, Ferencik M, Maurovich-Horvat P. Non-invasive and invasive imaging of vulnerable coronary plaque. Trends Cardiovasc Med. 2016; 26: 538–47.
16. Wildgruber M, Swirski FK, Zernecke A. Molecular Imaging of Inflammation in Atherosclerosis. Theranostics. 2013; 3: 865–84.
17. Cheng JM, Garcia-Garcia HM, de Boer SPM, et al. In vivo detection of high-risk coronary plaques by radiofrequency intravascular ultrasound and cardiovascular outcome: results of the ATHEROREMO-IVUS study. Eur Heart J. 2014; 35: 639–47.
18. Wilensky RL, Song HK, Ferrari VA. Role of Magnetic Resonance and Intravascular Magnetic Resonance in the Detection of Vulnerable Plaques. J Am Coll Cardiol. 2006; 47: C48–56.
19. Bezerra HG, Costa MA, Guagliumi G, Rollins AM, Simon DI. Intracoronary Optical Coherence Tomography: A Comprehensive Review. JACC Cardiovasc Interv. 2009; 2: 1035–46.
20. Erlinge D, Maehara A, Ben-Yehuda O, et al. Identification of vulnerable plaques and patients by intracoronary near-infrared spectroscopy and ultrasound (PROSPECT II): a prospective natural history study. The Lancet. 2021; 397: 985–95.
21. Ma J, Martin KH, Dayton PA, Jiang X. A preliminary engineering design of intravascular dual-frequency transducers for contrast-enhanced acoustic angiography and molecular imaging. IEEE Trans Ultrason Ferroelectr Freq Control. 2014; 61: 870–80.

22. Ma J, Martin KH, Li Y, et al. Design factors of intravascular dual frequency transducers for super-harmonic contrast imaging and acoustic angiography. Phys Med Biol. 2015; 60: 3441–57.

23. Peng C, Wu H, Kim S, Dai X, Jiang X. Recent advances in transducers for intravascular ultrasound (Ivus) imaging. Sensors. 2021; 21: 1–31.

24. Schoepf UJ, Becker CR, Ohnesorge BM, Yucel EK. CT of Coronary Artery Disease. Radiology. 2004; 232: 18–37.

25. Ghekiere O, Salgado R, Buls N, et al. Image quality in coronary CT angiography: challenges and technical solutions. Br J Radiol. 2017; 90: 20160567.

26. Wang J, Fleischmann D. Improving Spatial Resolution at CT: Development, Benefits, and Pitfalls. Radiology. 2018; 289: 261–2.

27. Slavin GS, Bluemke DA. Spatial and Temporal Resolution in Cardiovascular MR Imaging: Review and Recommendations. Radiology. 2005; 234: 330–8.

28. Varasteh Z, De Rose F, Mohanta S, et al. Imaging atherosclerotic plaques by targeting Galectin-3 and activated macrophages using (^{89}Zr)-DFO- Galectin3-F(ab')$_2$mAb. Theranostics. 2021; 11: 1864–76.

29. Tarkin JM, Joshi FR, Rudd JHF. PET imaging of inflammation in atherosclerosis. Nat Rev Cardiol. 2014; 11: 443–57.

30. Huang SW, Kim K, Witte RS, Olafsson R, O'Donnell M. Inducing and imaging thermal strain using a single ultrasound linear array. IEEE Trans Ultrason Ferroelectr Freq Control. 2007; 54: 1718–20.

31. Mahmoud AM, Dutta D, Lavery L, Stephens DN, Villanueva FS, Kim K. Noninvasive detection of lipids in atherosclerotic plaque using ultrasound thermal strain imaging: In vivo animal study. J Am Coll Cardiol. 2013; 62: 1804–9.

32. Seo CH, Shi Y, Huang S-W, Kim K, O'Donnell M. Thermal strain imaging: a review. Interface Focus. 2011; 1: 649–64.

33. Zeng W, Krueger JC, Dai Z. Ultrasonic Thermal Strain Imaging for Noninvasive Temperature Estimation in Tissue. ADVANCED ULTRASOUND IN DIAGNOSIS AND THERAPY. 2018; 2: 71.

34. Kim K, Huang SW, Hall TL, Witte RS, Chenevert TL, O'Donnell M. Arterial vulnerable plaque characterization using ultrasound-induced thermal strain imaging (TSI). IEEE Trans Biomed Eng. 2008; 55: 171–80.

35. Stephens D, Mahmoud A, Ding X, et al. Flexible integration of high-imaging- resolution and high-power arrays for ultrasound-induced thermal strain imaging (US-TSI). IEEE Trans Ultrason Ferroelectr Freq Control. 2013; 60: 2645–56.

36. Nguyen MM, Ding X, Leers SA, Kim K. Multi-Focus Beamforming for Thermal Strain Imaging Using a Single Ultrasound Linear Array Transducer. Ultrasound Med Biol. 2017; 43: 1263–74.

37. Khalid WB, Chen X, Kim K. Multifocus Thermal Strain Imaging Using a Curved Linear Array Transducer for Identification of Lipids in Deep Tissue. Ultrasound Med Biol. 2021; 47: 1711–24.

38. Krejza J, Arkuszewski M, Kasner SE, et al. Carotid Artery Diameter in Men and Women and the Relation to Body and Neck Size. Stroke. 2006; 37: 1103–5.

39. Chen M, Sheng Z, Kim H, et al. Design and Simulation of Heating Transducer Arrays for Ultrasound-Induced Thermal Strain Imaging. In: 2021 IEEE International Ultrasonics Symposium (IUS). IEEE; 2021.

40. Chen HC, Patel V, Wiek J, Rassam SM, Kohner EM. Vessel diameter changes during the cardiac cycle. Eye. 1994; 8: 97–103.

41. Krejza J, Arkuszewski M, Kasner SE, et al. Carotid Artery Diameter in Men and Women and the Relation to Body and Neck Size. Stroke. 2006; 37: 1103–5.

42. Chen M, Sheng Z, Kim H, et al. Design and Simulation of Heating Transducer Arrays for Ultrasound-Induced Thermal Strain Imaging. In: 2021 IEEE International Ultrasonics Symposium (IUS). IEEE; 2021.

43. Bagavathiappan S, Lahiri BB, Saravanan T, Philip J, Jayakumar T. Infrared thermography for condition monitoring - A review. Vol. 60, Infrared Physics and Technology. 2013.

44. Odéen H, Parker DL. Magnetic resonance thermometry and its biological applications – Physical principles and practical considerations. Prog Nucl Magn Reson Spectrosc. 2019; 110: 34–61.

45. Winter L, Oberacker E, Paul K, et al. Magnetic resonance thermometry: Methodology, pitfalls and practical solutions. International Journal of Hyperthermia. 2016; 32: 63–75.

46. Bajzek TJ. Thermocouples: a sensor for measuring temperature. IEEE Instrum Meas Mag. 2005; 8: 35–40.

47. Chen M, Zhang B, Kim H, et al. Millisecond-Level Transient Temperature Monitoring Using an Ultra-Fast Response Thermocouple for Ultrasound-Induced Thermal Strain Imaging. In: 2022 IEEE International Ultrasonics Symposium (IUS). IEEE; 2022.

48. Kim J, Lindsey BD, Chang W-Y, et al. Intravascular forward-looking ultrasound transducers for microbubble-mediated sonothrombolysis. Sci Rep. 2017; 7: 3454.

49. Politano A, Chiarello G. Probing the Young's modulus and Poisson's ratio in graphene/metal interfaces and graphite: a comparative study. Nano Res. 2015; 8: 1847–56.

50. Pierson HO. Handbook of Carbon, Graphite, Diamonds and Fullerenes Processing, Properties and Applications. William Andrew; 1994.

51. U.S. Food and Drug Administration. Marketing Clearance of Diagnostic Ultrasound Systems and Transducers Guidance for Industry and Food and Drug Administration Staff. 2019.

52. Kim H, Wu H, Chen M, Dai X, Zhou R, Jiang X. Intravascular Sono-Ablation for In-Stent Restenosis Relief: Transducer Development and the In-Vitro Demonstration. IEEE Trans Biomed Eng. 2023; 1–9.

53. Chakraborty DP, Brezovich IA. Error sources affecting thermocouple thermometry in RF electromagnetic fields. Journal of Microwave Power. 1982; 17: 17–28.

54. Tiennot T, Kamimura HAS, Lee SA, Aurup C, Konofagou EE. Numerical modeling of ultrasound heating for the correction of viscous heating artifacts in soft tissue temperature measurements. Appl Phys Lett. 2019; 114: 203702.

55. Billard BE, Hynynen K, Roemer RB. Effects of physical parameters on high temperature ultrasound hyperthermia. Ultrasound Med Biol. 1990; 16: 409–20.

Supplementary Information

Millisecond-level transient heating and temperature monitoring technique for ultrasound-induced thermal strain imaging

Mengyue Chen[1, *], Zhiyu Sheng[2, *], Ran Wei[3], Bohua Zhang[1, 5], Howuk Kim[1, 6], Huaiyu Wu[1], Yu Chu[1], Qiyang Chen[3], Andrew Breon[4], Sibo Li[5], Matthew B. Wielgat[7], Dhanansayan Shanmuganayagam[7,8,9], Edith Tzeng[10], Xuecang Geng[4], Kang Kim[2, 3, †], Xiaoning Jiang[1, †]

[*] These authors equally contributed to this work

[†] Corresponding author. Email: kangkim@upmc.edu, xjiang5@ncsu.edu

[1]Department of Mechanical and Aerospace Engineering, North Carolina State University, Raleigh, NC, USA

[2]Department of Medicine, University of Pittsburgh, Pittsburgh, PA, USA

[3]Department of Bioengineering, University of Pittsburgh, Pittsburgh, PA, USA

[4]Blatek Inc., Boalsburg, PA, USA

[5]Shenqi Medical (USA) Sirius Technologies Ltd., Boston, MA, USA

[6]Department of Mechanical Engineering, Inha University, Incheon, South Korea

[7]Department of Animal and Dairy Sciences, University of Wisconsin-Madison, Madison, WI, USA

[8]Department of Surgery, University of Wisconsin School of Medicine and Public Health, Madison, WI, USA

[9]Center for Biomedical Swine Research & Innovation, University of Wisconsin-Madison, Madison, WI, USA

[10]Department of Surgery, University of Pittsburgh, Pittsburgh, PA, USA

This PDF file includes:

- supplementary tables S1 to S5
- supplementary figures S1 to S5

TABLE S1. SUMMARY OF HEATING ULTRASOUND TRANSDUCER IN CURRENT US-TSI DEVICES.

Author	Year	Test	Target	Transducer	Frequency*	Intensity†	Tempera-ture rise	Heating duration	Heating volume**	Refer-ences
Huang et al	2007	*In vitro*	Phantom	32-element array	6.7 MHz	320 W/cm^2 I_{SPPA}	1.0 °C	1.1 s	N/A	[30]
Liang et al	2008	*In vitro*	Phantom	128-element, linear array (Ultrasonix L14-5W/60)	5.6 MHz	195 W/cm^2 I_{SPPA}	1.7 °C	2000 s	N/A	[56]
Kim et al	2008	*In vitro*	Porcine artery	513-element, 2D phased array	1.0 MHz	2000 W/cm^2 I_P	3.2 °C	2.0 s	5 x 5 x 10 mm^3	[34]
Stephens et al	2013	*In vitro*	Phantom	6 single-element, flat or spherical aperture	3.5 MHz 4.0 MHz	56 W/cm^2 I_P 40 W/cm^2 I_P	3.0 °C	2.0 s	2 x 8 x 5 mm^3	[35]
Mahmoud et al	2013	*In vivo*	New Zealand white rabbits	Custom array	3.55 MHz	N/A	1.1 ± 0.1 °C	5.0 s	N/A	[31]
Mahmoud et al	2014	*Ex vivo*	Mouse livers	6 single-element	3.55 MHz	117 W/cm^2 I_{SPPA}	1.5 °C	3.0 s	N/A	[57]
Foiret et al	2015	*In vitro*	Phantom	1 single-element (Valpey-Fischer IL0508HP)	5.0 MHz	N/A	3.8 °C	30 s	0.9 x 0.9 mm^2	[58]
Nguyen et al	2017	*In vitro*	Phantom	Linear array (Philips ATL L7-4)	5.0 MHz	1040 W/cm^2 I_P	0.3 °C	2.0 s	8.5 x 10 mm^2	[36]
Khalid et al	2021	*In vitro*	Phantom	Curved linear array (Philips ATL C4-2)	3.0 MHz	354 W/cm^2 I_{SPPA}	1.0 °C	2.0 s	14 x 64 mm^2	[37]
Khalid et al	2021	*In vitro*	Phantom	Custom array	3.55 MHz	66 W/cm^2 I_{SPPA}	1.5 °C	3.0 s	8 x 5 mm^2	[59]
Our work‡	2024	*In vitro* *In vivo*	Phantom Pig	32-element, dual 1D concave arrays	3.5 MHz	1300 W/cm^2 I_{SPPA}	3.9 °C 2.0 °C	25 ms 50 ms	2 x 10 x10 mm^3	N/A

* I_{SPPA} refers to spatial peak pulse average intensity, and I_P refers to spatial peak intensity.

† Heating volume was represented in elevation× lateral x depth directions or lateral x depth directions.

‡ For *in vitro* tests, a 3.9 °C temperature rise was obtained within 25 ms of heating in phantom; for *in vivo* tests, a 2.0 °C temperature rise was obtained within 50 ms of heating in pig.

TABLE S2 MATERIAL PROPERTIES OF FINITE ELEMENT SIMULATION

Properties	PZT-5A	Properties	Al_2O_3/Epoxy	Graphite
Density	7750 kg/m^3	Density	2700 kg/m^3	2260 kg/m^3
C_{33}^E	111 GPa	Young's modulus	11.5 GPa	36.5 GPa
e_{33}	15.8 C/m^2	Poisson's ratio	0.32	0.19

TABLE S3 PERFORMANCE COMPARISONS OF HEATING TRANSDUCER ELEMENTS

	Material: PZT 5A	Material: PZT 5H	Material: PMN-PT
Impedance analysis	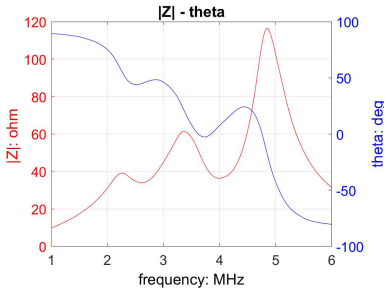	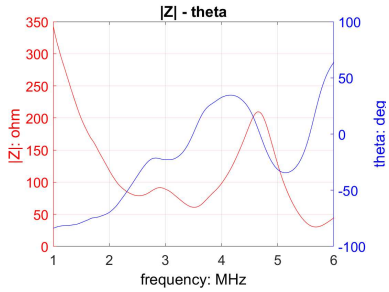	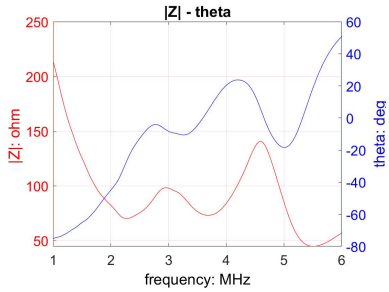
	Impedance (@ 3.5 MHz): 58 Ω Phase angle (@ 3.5 MHz): 8.6°	Impedance (@ 3.5 MHz): 62 Ω Phase angle (@ 3.5 MHz): 0.9°	Impedance (@ 3.5 MHz): 78 Ω Phase angle (@ 3.5 MHz): -4.9°
Pulse echo test	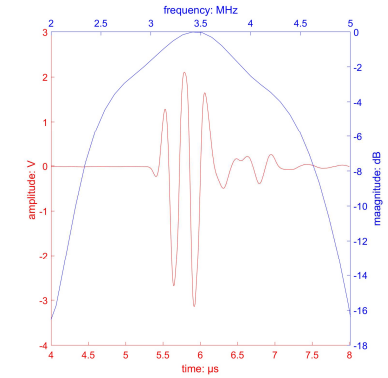	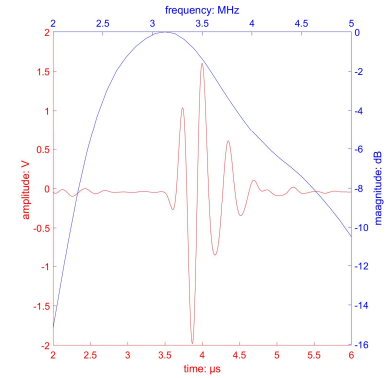	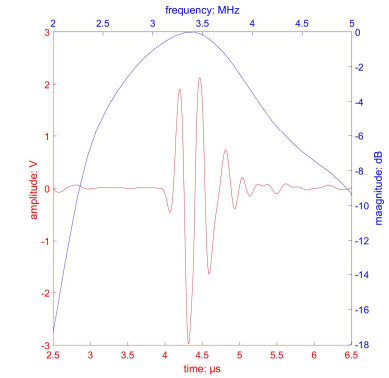
	Center frequency: 3.47 MHz Bandwidth (-6 dB): 60.3% Loop sensitivity: -15.6 dB	Center frequency: 3.27 MHz Bandwidth (-6 dB): 56.0% Loop sensitivity: -18.9 dB	Center frequency: 3.37 MHz Bandwidth (-6 dB): 57.0% Loop sensitivity: -15.8 dB
Hydrophone test	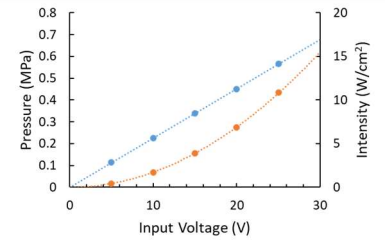	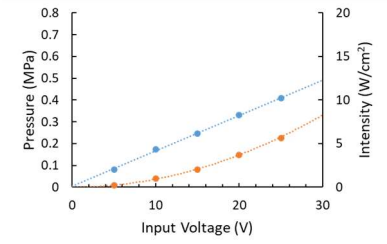	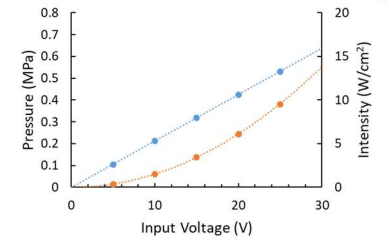
	Transmitting sensitivity (@ 5 cycles): 22.67 kPa/V	Transmitting sensitivity (@ 5 cycles): 16.34 kPa/V	Transmitting sensitivity (@ 5 cycles): 21.23 kPa/V

TABLE S4 SPECIFICATION OF UTILIZED THERMOCOUPLES

Item	Thermocouple No. 1	Thermocouple No. 2
Model	Ultra-fast response bare foil thermocouple	CO2-T
Manufacturer	RdF Corporation, NH, USA	Omega Engineering, Inc., CT, USA
Response time	1 - 5 ms	2 - 5 ms
Foil Thickness	12.7 μm (0.0005”)	12.7 μm (0.0005”)
Temperature range	-195.56 - 371.11°C	< 150.00°C
Total length	150 mm (6”)	150 mm (6”)

TABLE S5 ELECTRICAL IMPEDANCE SPECTRUM OF EACH HEATING ELEMENT

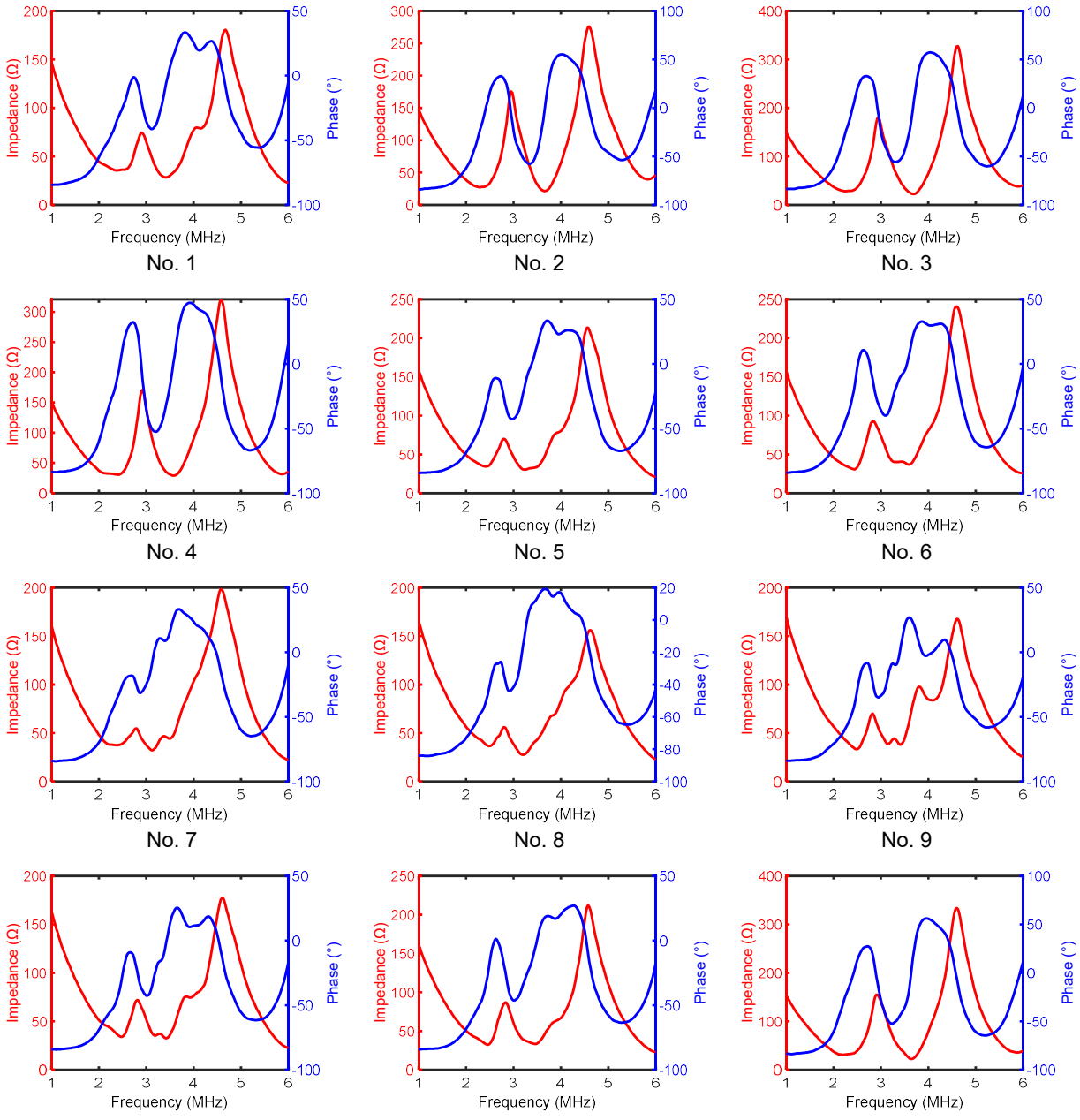

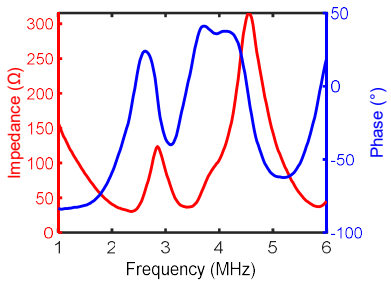

No. 13

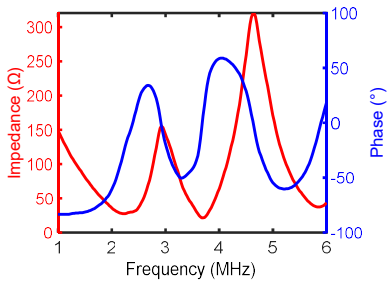

No. 14

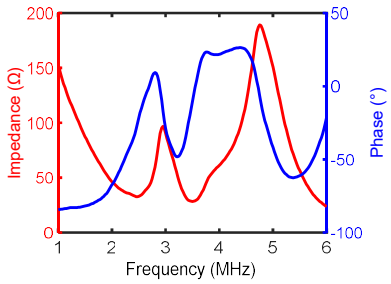

No. 15

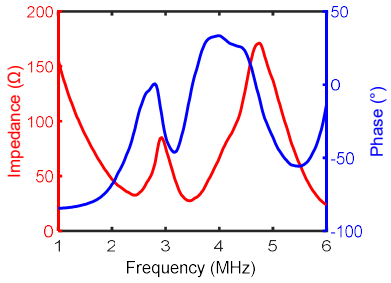

No. 16

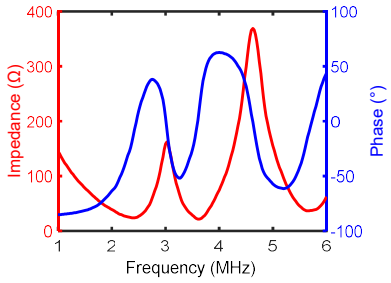

No. 17

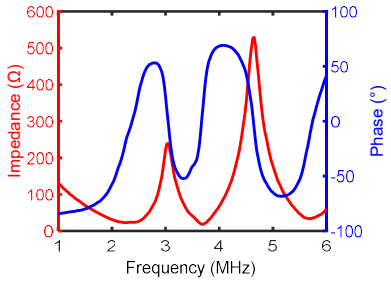

No. 18

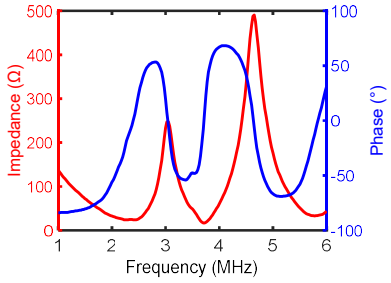

No. 19

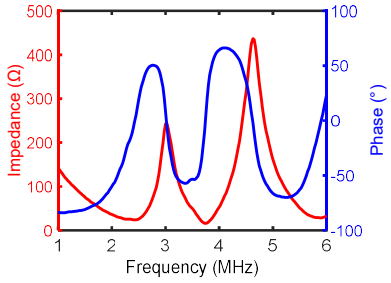

No. 20

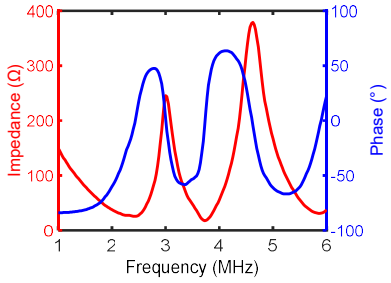

No. 21

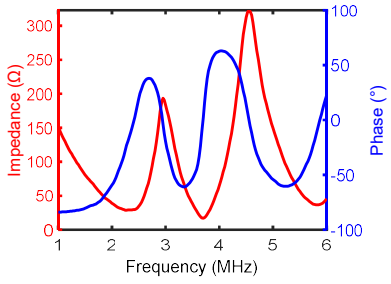

No. 22

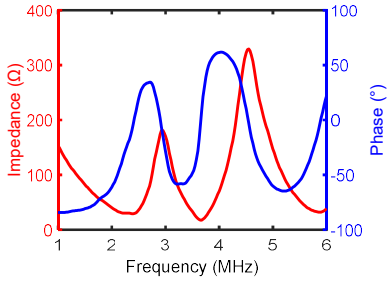

No. 23

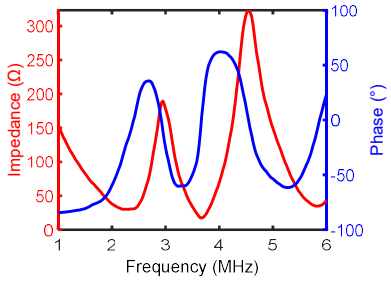

No. 24

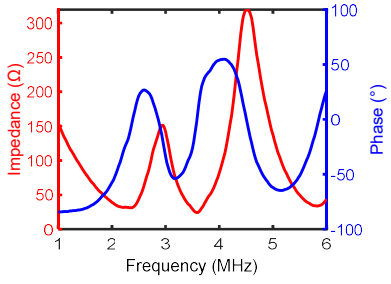

No. 25

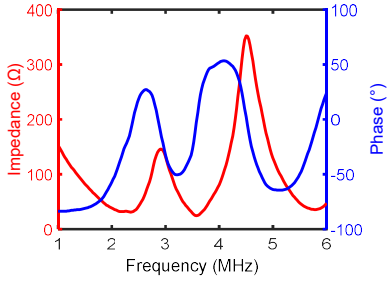

No. 26

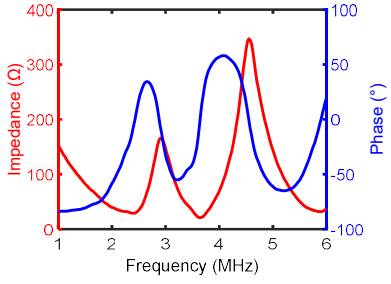

No. 27

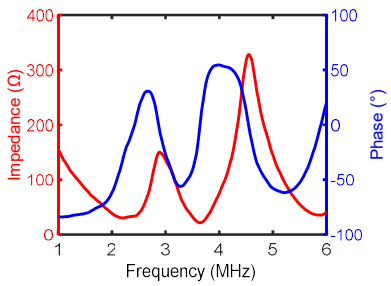

No. 28

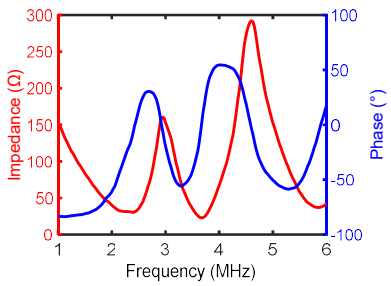

No. 29

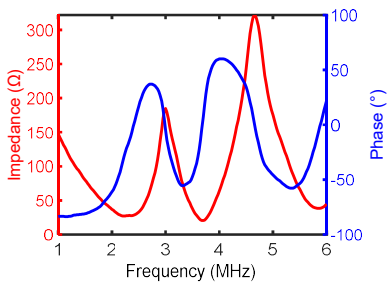

No. 30

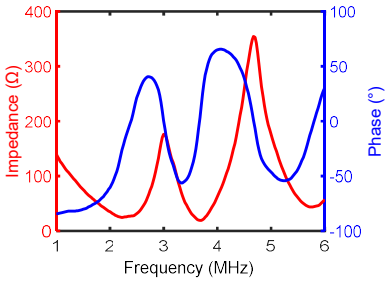

No. 31

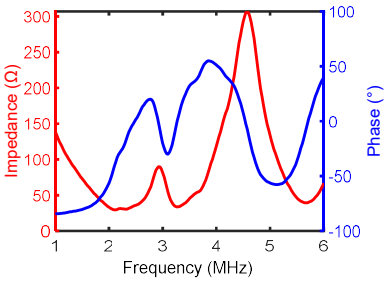

No. 32

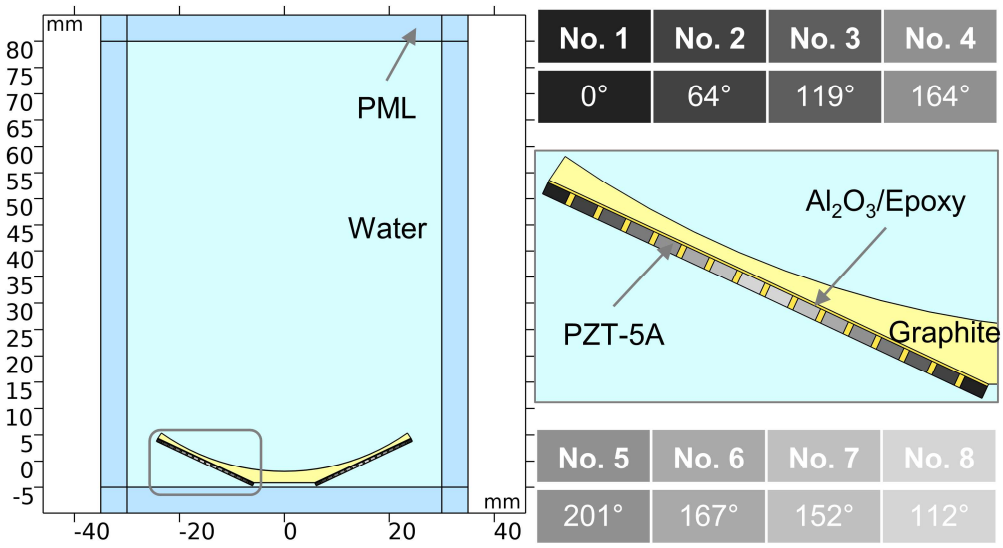

Figure S1. Acoustic simulation modeling for the heating transducer, with multi-focus beamforming applied by programming phase delay on each heating element.

A B

Figure S2. Photo of experiment setup for *in vivo* animal tests.

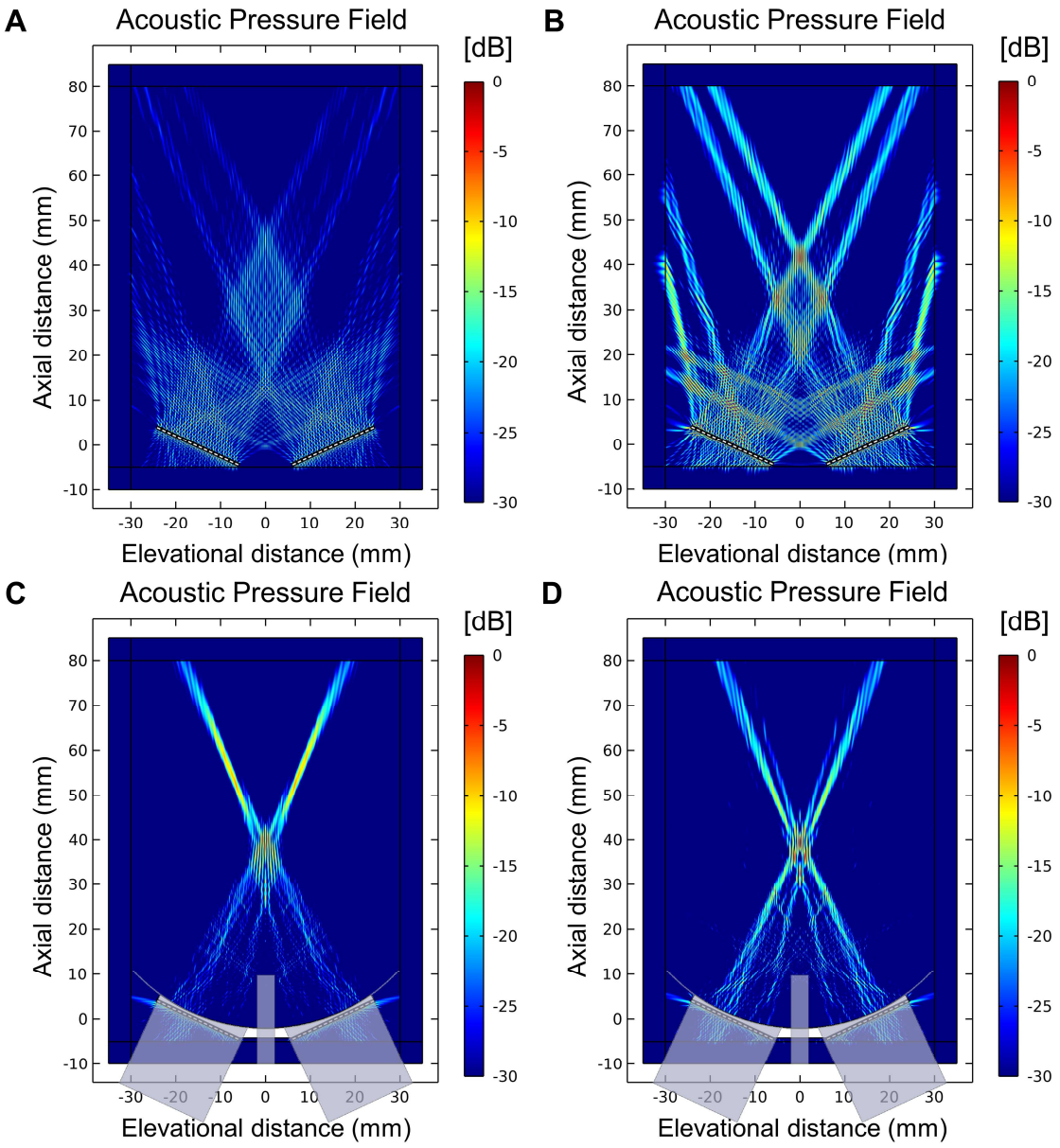

Figure S3. Simulated acoustic pressure field of the designed heating transducer in the YZ plane, including (A) not applying acoustic lens neither phase delay; (B) applying phase delay but not acoustic lens; (C) applying acoustic lens but not phase delay; (D) applying both acoustic lens and phase delay.

The absence of phase delay and acoustic lens clearly resulted in broad ultrasound beams (Figure S3A) lacking the beam focusing necessary to elevate acoustic pressure. The desired multi-focus beamforming could be achieved once the phase delay was applied to each heating element, as depicted in Figure S3B. Nevertheless, the lack of an acoustic lens contributed to a wide region of low acoustic pressure between each focal point. When only the acoustic lens was applied to the heating transducer, the simulated acoustic pressure field (Figure S3C) showed that there is a relatively high-pressure area generated at a focal depth of approximately 35 mm. However, two higher acoustic pressure regions were observed behind the intended focal area due to the absence of the necessary phase delay. When both acoustic lens and phase delay were applied, the simulated results (Figure S3D) demonstrated that the focal area of a single heating array overlapped with the other very well. The generated focal area of dual heating arrays had an approximate -12 dB beamwidth of 10 mm.

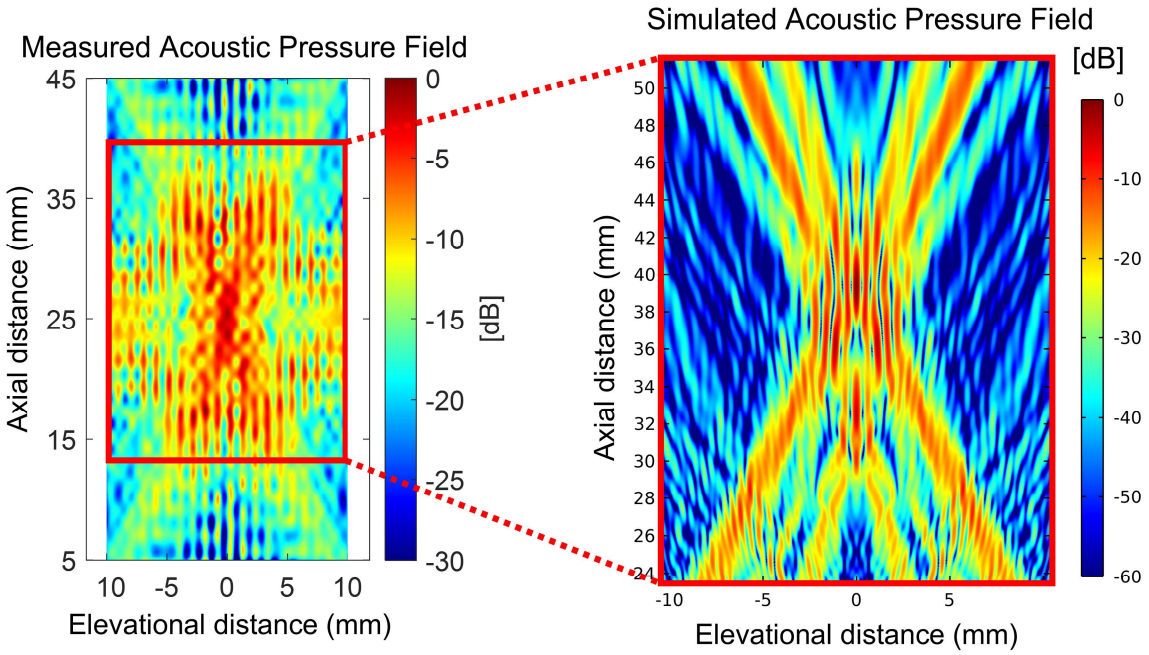

Figure S4. Comparison between measured and simulated acoustic pressure field of the designed heating transducer in YZ plane. Note that the coordinate systems for the simulated and measured acoustic pressure maps differ. In the measured map, the focal spot is located at an axial distance of 25 mm, whereas in the simulated map, it is at 35 mm.

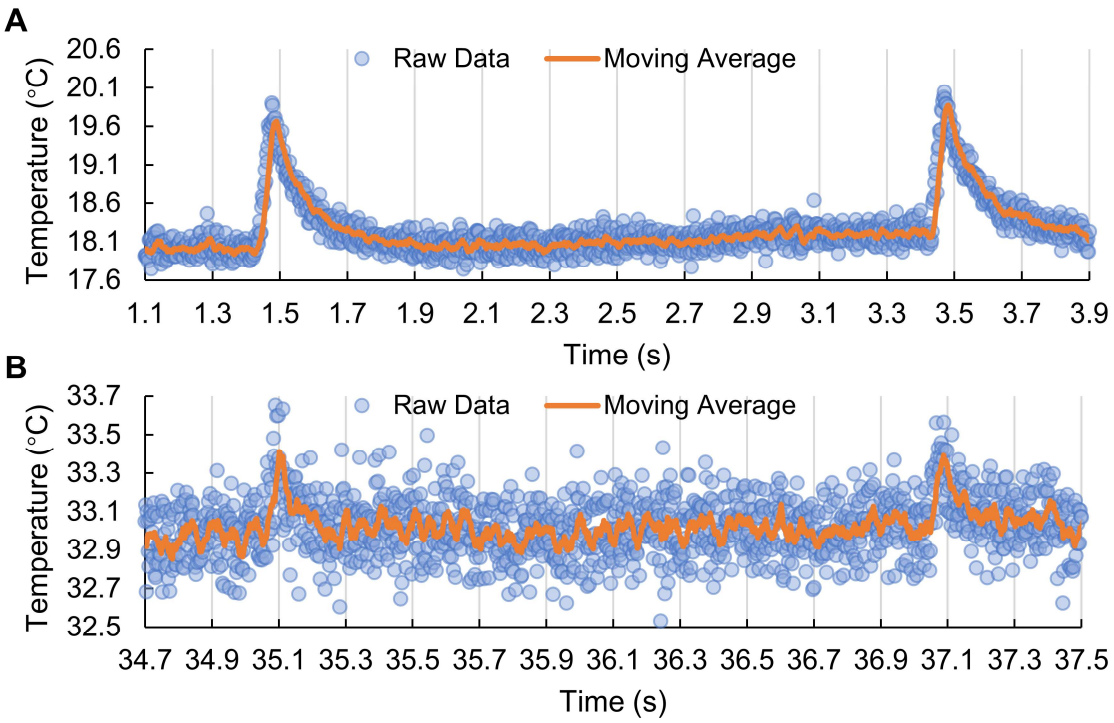

Figure S5. Measured transient temperature curve using fast-response thermocouple in (A) laser-induced thermal tests and (B) ultrasound-induced thermal tests.

References

56. Liang H-D, Zhou L-X, Wells PNT, Halliwell M. Temperature Measurement by Thermal Strain Imaging with Diagnostic Power Ultrasound, with Potential for Thermal Index Determination. Ultrasound Med Biol. 2009; 35: 773–80.

57. Mahmoud AM, Ding X, Dutta D, Singh VP, Kim K. Detecting hepatic steatosis using ultrasound-induced thermal strain imaging: An ex vivo animal study. Phys Med Biol. 2014; 59: 881–95.

58. Foiret J, Ferrara KW. Spatial and Temporal Control of Hyperthermia Using Real Time Ultrasonic Thermal Strain Imaging with Motion Compensation, Phantom Study. Talkachova A, Ed. PLoS One. 2015; 10: e0134938.

59. Khalid WB, Farhat N, Lavery L, Jarnagin J, Delany JP, Kim K. Non-invasive Assessment of Liver Fat in ob/ob Mice Using Ultrasound-Induced Thermal Strain Imaging and Its Correlation with Hepatic Triglyceride Content. Ultrasound Med Biol. 2021; 47: 1067–76.